

**Reaction dynamics and in-medium nucleon-nucleon cross section with  $^{12}\text{C} + ^1\text{H}$  at 95 MeV/nucleon**G. Tian<sup>1</sup>, Z. Chen<sup>1,2,\*</sup>, R. Wada<sup>3,†</sup>, X. Liu<sup>4</sup>, W. Lin<sup>4</sup>, M. Huang<sup>5</sup>, H. Zheng<sup>6</sup>, Q. Hu<sup>1,2</sup>, R. Han<sup>1,2</sup>, F. Shi<sup>1</sup>, X. Zhang<sup>1,2</sup>, B. Liu<sup>1,2</sup>, and H. Sun<sup>1,2</sup><sup>1</sup>*Institute of Modern Physics, Chinese Academy of Sciences, Lanzhou 730000, China*<sup>2</sup>*School of Nuclear Science and Technology, University of Chinese Academy of Sciences, Beijing 100049, China*<sup>3</sup>*Cyclotron Institute, Texas A&M University, College Station, Texas 77843, USA*<sup>4</sup>*Key Laboratory of Radiation Physics and Technology of the Ministry of Education, Institute of Nuclear Science and Technology, Sichuan University, Chengdu 610064, China*<sup>5</sup>*College of Mathematics and Physics, Inner Mongolia Minzu University, Tongliao 028000, China*<sup>6</sup>*School of Physics and Information Technology, Shaanxi Normal University, Xi'an 710119, China*

(Received 22 December 2022; accepted 17 March 2023; published 5 April 2023)

Reaction dynamics and effective in-medium nucleon-nucleon ( $NN$ ) cross section are studied, using the antisymmetrized molecular dynamics (AMD) model with one of the simplest heavy ion collisions,  $^{12}\text{C} + ^1\text{H}$ . The roles of different stochastic processes are studied, which are installed in the original AMD. One is the diffusion process as a part of the quantum fluctuation originated from the Fermi motion during the time evolution of the wave packets in the mean field (AMD/D). The second is a coalescence treatment for light clusters with  $A \leq 8$  (AMD/D-COALS). The third is the collision process, installed in AMD with different form of the in-medium  $NN$  cross sections. These different processes are examined, using the experimental angular distributions and energy spectra of light charged particles and intermediate mass fragments. The effective in-medium  $NN$  cross sections are evaluated from the simulated AMD events and compared with the experimentally extracted values. A good agreement is obtained between the AMD values from the  $^{12}\text{C} + ^1\text{H}$  reaction at 95 MeV/nucleon and the experimental results for nuclear matter.

DOI: [10.1103/PhysRevC.107.044602](https://doi.org/10.1103/PhysRevC.107.044602)**I. INTRODUCTION**

Transport models provide a powerful tool to obtain physics information on the nuclear equation of state and in-medium properties from low to relativistic energy heavy-ion collisions, which produce a variety of different nuclear matter in temperature, density, and neutron/proton ratio together with a variety of reaction dynamics. A recent review of various transport models in the transport model evaluation project (TEMP), with calculations under controlled conditions of physical input and setup, reveals that the differences in the basic feature of all models from the Boltzmann-Uehling-Uhlenbeck (BUU) type to the quantum molecular dynamics (QMD) type can be understood, whereas detailed comparisons of the actual observables, pion productions for example, show significant differences [1–5]. One of the main causes for the differences originates from the differences in managing the Pauli blocking in the stochastic collision process. In the following study we adopt the antisymmetrized molecular dynamics (AMD) of Ono [6], in which the Pauli blocking is treated in an exact manner.

The original code of AMD based on Ref. [6], however, showed a significant transparency of the projectile through the

target nucleus even for central collisions of  $^{40}\text{Ca} + ^{40}\text{Ca}$  at 35 MeV/nucleon, and resulted in a significant enhancement of the projectilelike yields in the charge distribution, which was not observed in the experiment. To resolve this, a quantum diffusion process was introduced. This version of AMD, called AMD/D, made a significant improvement to describe the multifragmentation events [7–9].

Another significant improvement was made by the incorporation of the coalescence process. The coalescence process was first introduced to describe the intermediate mass fragment production in  $^{197}\text{Au} + ^{197}\text{Au}$  at 150 and 250 MeV/nucleon [10]. In a series of our previous studies in Refs. [11–13], the coalescence process with  $A \leq 4$  were studied in the  $^{12}\text{C} + ^{12}\text{C}$  reaction at 50 and 95 MeV/nucleon. This version of AMD reproduced the general trends of the basic observables rather well, such as the angular distributions and energy spectra for light charged particles (LCPs) and intermediate mass fragments (IMFs) up to  $Z \leq 12$ . However, the detailed comparisons revealed that for some particle species the AMD predictions showed noticeable deviations from the experimental data. Their origins were not able to be pinned down in these studies because of the complicated mechanism of the heavy ion collisions, even though the  $^{12}\text{C} + ^{12}\text{C}$  system is a rather simple reaction system.

In addition we study the effective in-medium nucleon-nucleon ( $NN$ ) cross sections in the present work. Here the effective in-medium  $NN$  cross section refers to that

\*zqchen@impcas.ac.cn

†wada@comp.tamu.edu

evaluated from the AMD simulations to distinguish from the input in-medium  $NN$  cross section. Historically in AMD different in-medium cross sections have been applied: the free  $NN$  cross sections [14] for high energy application and the Li-Machleidt formalism with an empirical formula used as an upper limit below certain energies [10]. There are also other forms of the cross sections available in the code. In experiments, the in-medium  $NN$  cross section has been evaluated from a series of nuclear stopping studies with different symmetric reactions in the incident energy range of 20–100 MeV/nucleon [15–17]. However, these experimentally extracted in-medium  $NN$  cross sections are difficult to compare directly to the input  $NN$  cross section used in the simulations, because many of the attempted collisions calculated from the input in-medium cross section are Pauli blocked. We propose a simple method to calculate the “effective” in-medium cross sections from the simulations to compare with the experimental values.

AMD is one of the state-of-art transport models, but still has problems reproducing the experimental data in many cases. Some of the discrepancies between the simulated results and those of the experiments originate from the missing physics in its ingredients. They have often different origins depending on the ejectile energies and species as well as the different reaction systems and incident energies, as described above for some of them. However some discrepancies may originate not from physics, but from from the experimental procedures. In order to identify them, one needs to characterize the nature of the ingredients. However heavy ion collisions are very complicated in general and it is often very difficult to isolate individual roles of the ingredients incorporated in the program. In this study we chose  $^{12}\text{C} + ^1\text{H}$  at 95 MeV/nucleon, which is one of the simplest heavy ion collisions, but still shows many aspects of the reaction dynamics.

This article is organized as follows: In Sec. II, AMD models used in this study are described briefly. In Sec. III, simulated results are compared with the experimental data of Dudouet *et al.* in Ref. [18]. Discussions on the coalescence model and the production mechanisms of protons are given in Sec. IV. The effective in-medium  $NN$  cross sections are also discussed. A brief summary is given in Sec. V.

## II. ANTISYMMETRIZED MOLECULAR DYNAMICS MODELS

Since general descriptions of AMD have been provided in Refs. [6,7,10,12,13], only parts related to this study are given in detail in this section.

### A. AMD/D

To take into account the fluctuation in the time evolution of the wave packet, a quantum branching process is introduced along to path of the Vlasov equation [7]. This quantum diffusion process is a generalized process of the momentum fluctuation introduced to restore a quantum nature in the particle emission process in their earlier studies [19,20].

This version of AMD improved the reproduction of IMF's significantly.

### B. AMD/D-COALS

In AMD/D, a stochastic coalescence process can be activated. The coalescence process was introduced to improve the production of clusters in  $^{197}\text{Au} + ^{197}\text{Au}$  at 150 and 250 MeV/nucleon [10]. The basic procedures are as follows. At each time step, candidate clusters with  $A \leq 4$  are formed with a given coalescence radius  $R_c$ . In the default routine,  $R_c = 1.5$  fm is used. For the deuteron case, for example, when a coalescence process takes place, this stochastic process moves the centroids  $\mathbf{Z}_a$  and  $\mathbf{Z}_b$  to the same point  $\frac{1}{2}(\mathbf{Z}_a + \mathbf{Z}_b)$ . The rate of the coalescence  $c$  is automatically determined by the requirement that the probability of finding the two nucleons in the deuteron state  $|d\rangle$  should be independent of time on average. Similar treatment is performed for tritons,  $^3\text{He}$ , and  $\alpha$  particles. First all possible candidate cluster combinations are formed for  $A \leq 4$ . If the multiplicity of the candidate clusters is more than or equal to 2, a heavier cluster formation with  $A > 4$  is attempted between two candidate clusters. No three-candidate cluster formation is applied in this work.

The formed cluster is further examined to satisfy the following conditions.

- (i) The nucleons in the attempted cluster should not be a part of heavier clusters.
- (ii) The cluster should not exist in the previous time step.
- (iii) The cluster should be formed in a low density region.
- (iv) The total energy should be restored.
- (v) The final state should be allowed under the Pauli principle.

When the attempted cluster satisfies the above conditions, the coalescence process is performed. Otherwise, no change is made in the system.

The coalescence process also affects kinematically and thermally in the system. When a cluster is formed, the excitation energy of the cluster is minimized because the relative kinetic energies are minimized in their rest frame, which reduces the excitation energy of the cluster. This is evident when the excitation energy is evaluated for the afterburner at the switching time. The kinetic energies of the cluster and nearby nucleons also change. It should be also noted that the formed cluster can breakup at later stages, since each nucleon in the cluster is treated as same as the other nucleons.  $NN$  collisions between one of nucleons in the cluster and the surrounding nucleons can occur and/or the independent time evolution of the participated nucleons in the cluster can break them up. In this study AMD/D with the coalesce process with  $A \leq 8$  is referred as AMD/D-COALS.

In Fig. 1 the probability of a successful coalescence process as a function of fragment mass is plotted for  $^{12}\text{C} + ^1\text{H}$  at 95 MeV/nucleon. In almost every event clusters with  $A = 2, 6, 7$  are successfully made on average.  $\alpha$  formation probability is ten times smaller than those of  $d$  and  $A = 6, 7$  clusters. One reason is that when an  $\alpha$  is formed, the nucleons inside the  $\alpha$  are strongly bounded and tend to stay together, whereas for

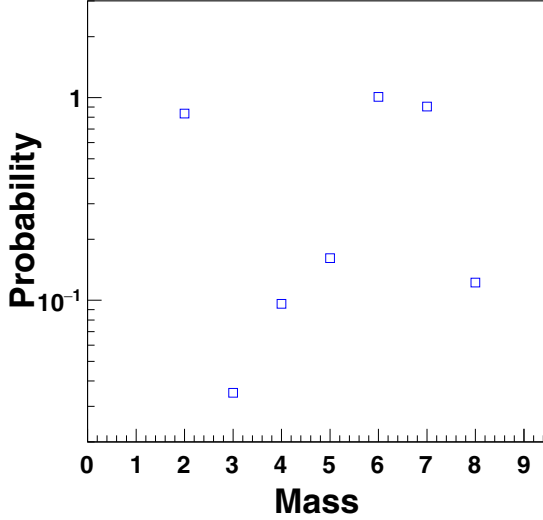


FIG. 1. Average occurrence of the coalescence process per event as a function of mass.

the other heavier clusters the formed cluster can be broken up and reformed again more than once in a given event.

### C. In-medium $NN$ cross section

In AMD calculations, the  $NN$  collision rate is, by default, determined by using the input in-medium cross section as [21]

$$\sigma(E, \rho) = \min\left(\sigma_{LM}(E, \rho), \frac{100 \text{ mb}}{1 + E/200}\right), \quad (1)$$

where  $\sigma_{LM}(E, \rho)$  is the in-medium cross section given by Li and Machleidt [22,23].  $E$  is the relative kinetic energy between two nucleons and given in MeV and  $\rho$  is the density. The angular distribution of proton-neutron scattering is parametrized as

$$\frac{d\sigma_{pn}}{d\Omega} \propto 10^{-\alpha(\pi/2 - |\theta - \pi/2|)},$$

$$\alpha = \frac{2}{\pi} \max\{0.333 \ln E - 1, 0\}, \quad (2)$$

while the angular distributions of proton-proton and neutron-neutron scatterings are assumed isotropic. The above in-medium cross section is applied in all calculations below, unless otherwise specified. For the in-medium  $NN$  cross section study in Sec. IV, free  $NN$  cross sections are also applied for comparisons.

### D. Simulations

In the following AMD simulations, the standard Gogny interaction is used, which has the incompressibility  $K = 228$  MeV [24]. The impact parameter range is set to  $b = 0-6$  fm, since very rare interaction occurs between the projectile and the target at  $b > 6$  fm. The time evolution is performed up to 300 fm/c, which has been verified as a reasonable time such that the dynamics of the collision process is already established for the final partitions [8]. To get the final products, the results are examined at  $t = 300$  fm/c using a coalescence

technique, and their excitation energies and spins are evaluated. For the excited fragments GEMINI [25,26] is employed as the afterburner to get the final products to compare with the experimental data.

## III. RESULTS

### A. Overview of experimental results

The experimental results used in this study were measured at GANIL in Ref. [18], using four sets of Si-Si-CsI telescopes at the laboratory angles of  $4^\circ, 7^\circ, \dots$  up to  $43^\circ$  in  $2^\circ$  steps. All experimental cross sections for the  $^{12}\text{C} + ^1\text{H}$  are obtained by combining the cross sections of  $^{12}\text{C} + \text{CH}_2$  and  $^{12}\text{C} + \text{C}$  as

$$\frac{d\sigma}{d\Omega}(\text{H}) = \frac{1}{2} \left( \frac{d\sigma}{d\Omega}(\text{CH}_2) - \frac{d\sigma}{d\Omega}(\text{C}) \right). \quad (3)$$

To visualize a global picture of the experimental data, the energy spectra of LCPs are fitted by a moving source (MS) fit with two sources, a projectilelike (PLF) source and an intermediate-velocity (IV) source, following the work in Ref. [11]. The PLF source further consists of two sources with different slopes, but with similar source velocities except for  $\alpha$  particles. For  $\alpha$  particles, a single PLF is sufficient to reproduce the spectra at all angles. The experimental energy spectra and typical MS fit results are shown in Fig. 2. The experimental energy spectra are well reproduced without a TLF source except for deuterons. For deuterons, most of the spectra shown in the second column in Fig. 2 suggest the existence of a possible TLF source around the energy below 20 MeV/nucleon. On the other hand, none of the proton and triton spectra show similar enhancements at similar energies. The spectra below 30-50 MeV/nucleon are well described by the IV source, especially for protons, the spectra at  $\theta > 20^\circ$  are dominated by the IV source. For  $\alpha$  particles, the detection energy threshold is too high to observe the IV source component experimentally.

### B. Overview of AMD results

In Fig. 3, two-dimensional (2D) plots of the velocity distributions,  $d^2\sigma/dV_t dV_z$ , where  $dV_t, dV_z$  are the transverse and parallel velocities, respectively, are shown for protons from different AMD simulations.  $V_t$  is set positive (negative) when  $V_y$  is positive (negative).

On the top row, the results from AMD without the diffusion process, denoted as AMD/noD, are presented for the primary (AMD alone) on the left and the secondary (AMD+GEMINI) on the right column. For the primary distribution, a clear ring is observed. The center velocity of the ring corresponds to that of the  $NN$  center of mass, a half beam velocity, and therefore it is formed by a quasielastic scattering between a nucleon in the projectile  $^{12}\text{C}$  nucleus and the target proton. No PLF source component is observed at this stage. When the primary fragments are cooled down by GEMINI on the right column, a clear PLF component appears around the beam velocity. This indicates that excited PLF fragments exist at the projectile velocity on the primary stage on the left, but no particle emissions are made from the excited PLFs before  $t = 300$  fm/c. On the second row, AMD/D results are shown.

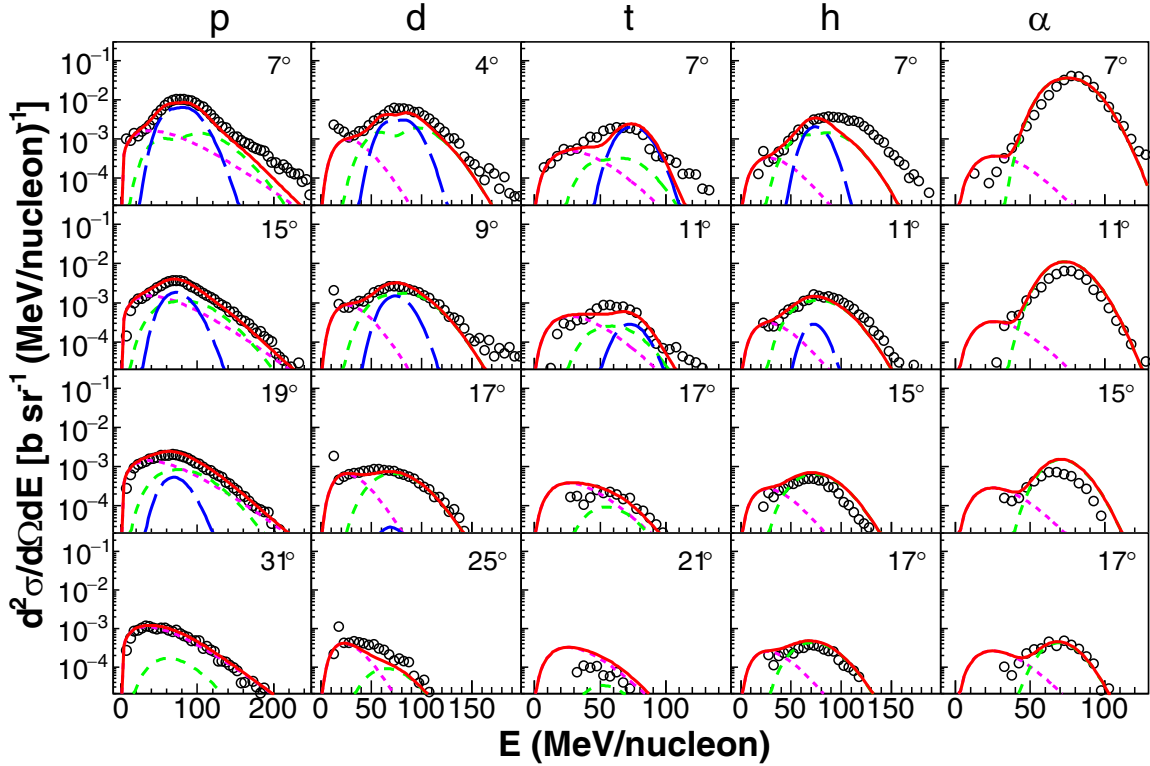


FIG. 2. Moving source fit results for  $p$ ,  $d$ ,  $t$ ,  ${}^3\text{He}$  (denoted as  $h$ ), and  $\alpha$  particles from the left column to the right at selected angles. The experimental data from Ref. [18] are shown by open circles. The PLF1, PLF2, and IV components are shown by blue long-dashed, green dashed, and pink dotted curves, respectively. The total sum of the components of the fit result is shown by the red solid curve. Polar laboratory angles,  $\theta$ , are shown in each figure.

The diffusion process made two noticeable changes: one is to broaden the width of the ring at the lower velocity side and the other to stimulate the particle emission from the excited PLFs. As addressed in Sec. II A, these are expected effects of the incorporated diffusion process. For the secondary distribution on the right, the PLF protons are further enhanced, indicating that the PLF excitation energy is only partially consumed for the emissions caused by the diffusion process and a significant amount remains at  $t = 300$  fm/c. On the third row, the results of AMD/D-COALS are presented. Noticeable differences of the primary distribution are observed, compared to that of AMD/D. The width of the ring is reduced when the proton velocity becomes closer to that of PLF. This can be explained as follows. When one of the quasielastically scattered protons is emitted near the rest of the projectile, this proton has more chance to form a cluster with nucleons in the projectile by a coalescence process, and the proton yields are reduced. The closer to the projectile, the higher probability is for the coalescence and the thinner the ring is. The yields of the PLF source are reduced at the primary stage, since the coalescence process reduces the excitation energy of the fragments in the PLF source, as mentioned in Sec. II B. The radius of the outer sphere at the forward direction is slightly enlarged, reflecting the enhancement of the high energy tails due to the contribution by the coalescence process as discussed in Sec. IV B.

### C. Quantitative comparisons

In Figs. 4 and 5, the experimental energy spectra of LCPs and IMFs are compared with the AMD+GEMINI results at selected angles. For protons in the leftmost column of Fig. 4, both AMD/D and AMD/D-COALS simulated results are very similar to each other and can reproduce more or less reasonably the experimental data with some deviations. AMD/D-COALS reproduces well the high energy tail above  $E > 150$  MeV/nucleon at all angles, whereas the spectra from AMD/D fall off much quickly in this energy region. In both simulations the yields near the projectile velocity are overpredicted. AMD/D also shows a sharp peak around  $E = 60\text{--}70$  MeV/nucleon, which corresponds to the energy of the quasielastic ring observed in Fig. 3. In Sec. IV B, these differences in the simulated proton spectra will be discussed in more detail.

For all other LCPs both AMD/D and AMD/D-COALS overpredict the yields around the projectile velocity at the forward angles, except for  ${}^3\text{He}$ . Since the  ${}^3\text{He}$  evaporation rate from the excited IMFs is small, compared to other clusters, these overpredictions are attributed to the sequential feeding process from the excited IMFs. The cause of these overpredictions is further discussed in Sec. IV in detail. AMD/D-COALS broadens noticeably the width of the energy spectra for deuterons, tritons, and  ${}^3\text{He}$  particles, and improves the reproduction of these energy spectra at all angles,

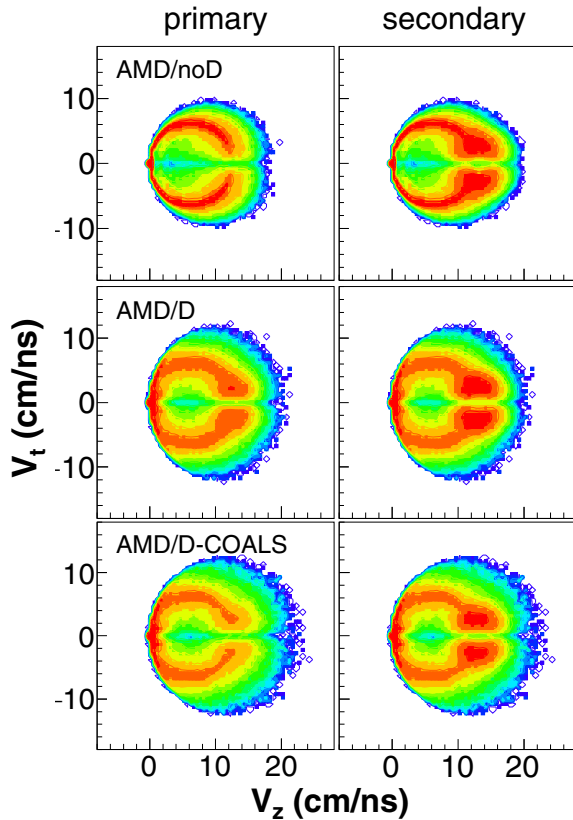


FIG. 3. 2D velocity distributions for protons are compared for AMD/noD, AMD/D, and AMD/D-COALS from the top to the bottom, respectively. The velocity spectra for the primary protons are plotted on the left column and those for the secondary on the right.

especially at the lower energy side of the spectra. The experimental yields of all LCPs show higher energy tails at  $\theta < 10^\circ$  which are not predicted by the AMD models. However, one should note that these experimental high energy tails are inconsistent with each other from angle to angle. For example, the high energy tail of  $\alpha$  particles is enhanced at  $7^\circ$  (second row) much more than those at  $4^\circ$  and  $9^\circ$ . Such inconsistencies are also seen in other LCPs. Therefore we suspect that these high energy tails above  $E > 200$  MeV/nucleon for protons and deuterons and  $E > 150$  MeV/nucleon for  $\alpha$  particles originate mainly from some errors in the experimental data analysis, such as the energy calibration at high energy and/or the spectrum subtraction method used in Eq. (3).

In Fig. 5, a similar comparison is made for IMFs. All simulated results except for the Li isotopes are reproduced more or less reasonably well compared to the experimental yields near the energy corresponding to the projectile velocity, but fail to describe them at  $E < 50$  MeV/nucleon. These discrepancies on the lower energy side between the experimental data and the simulations are difficult to explain, based on physics. For heavier target system, these IMFs are mainly from the target fragmentation, whereas in the present case of  $^{12}\text{C} + ^1\text{H}$  no such target source exists. One should note that the cross sections of these spectra in the lower energy region are more than two orders of magnitude smaller than the peak yields. As mentioned for LCPs above, these experimental energy spectra

are obtained from the subtraction between those of  $^{12}\text{C} + \text{CH}_2$  and  $^{12}\text{C} + \text{C}$ , using Eq. (3). Therefore, these low energy IMFs may be mainly produced during the experimental data analysis.

## IV. DISCUSSION

### A. LCP production

In our previous works [12,13], the role of the cluster correlations in the IMF emissions was addressed in detail, using the experimental results for  $^{12}\text{C} + ^{12}\text{C}$  at 50 and 95 MeV/nucleon from Refs. [27] and [18], respectively. The comparisons performed in the present study using the  $^{12}\text{C} + ^1\text{H}$  reaction in the inverse kinematics are qualitatively consistent with our previous works. Some of the LCP yields at the PLF velocity, however, are noticeably overpredicted as shown in Fig. 4 in the present and previous works. In the following we further study the production mechanisms of LCPs, focusing on the role of the coalescence process in more detail.

To study the overpredictions, the experimental energy spectra of tritons at  $4^\circ$  to  $9^\circ$  are compared with the simulations, where the different feeding contributions from heavier clusters are presented separately in Fig. 6. The energy spectra from both results are similar to each other. Even though the reproduction of the experimental data is not as good as we expected, the reproduction of the energy spectra in the low energy side is significantly improved by AMD/D-COALS at larger angles. The comparison between the two models reveals distinct differences in the production of tritons. In AMD/D, the feeding from Boron isotopes is dominated in the triton yields. In AMD/D-COALS, on the other hand, the primary contribution dominates the spectra and the feeding contributions are reduced significantly. This is because the coalescence process employed forms the clusters and emits them at the primary stage. The coalescence process also reduces the excitation energy of the IMFs as mentioned earlier. The noticeable improvement for AMD/D-COALS at larger angles is also evident in Fig. 4 for other LCPs except  $\alpha$  particles. For  $\alpha$  particles, AMD/D reproduces results slightly better than AMD/D-COALS at two forward angles. The overpredictions of the Li isotopes in AMD/D-COALS observed in Fig. 5 does not contribute to the LCP production as observed in the triton case. This is because most of the Li isotopes generated by the coalescence process have little excitation energy and do not decay noticeably into LCPs.

### B. Proton emission and effective in-medium $NN$ cross section

In Fig. 7, proton energy spectra are shown with AMD predictions. In AMD/D and AMD/D-COALS the default in-medium  $NN$  cross section in Eq. (1) is used, whereas in AMD/D-COALS(FX) the parametrized free  $NN$  cross sections are used for comparisons. At peak energy the former two predict very similar yields, but show noticeable difference at high energy tails. In our previous study of the high energy proton emission in Ref. [28], the incorporated Fermi boost plays a dominant role in reproducing the high energy protons in  $^{40}\text{Ar} + ^{51}\text{V}$  at 44 MeV/nucleon. For  $^{12}\text{C} + ^1\text{H}$  at 95 MeV/nucleon, however, no effect is observed for the Fermi

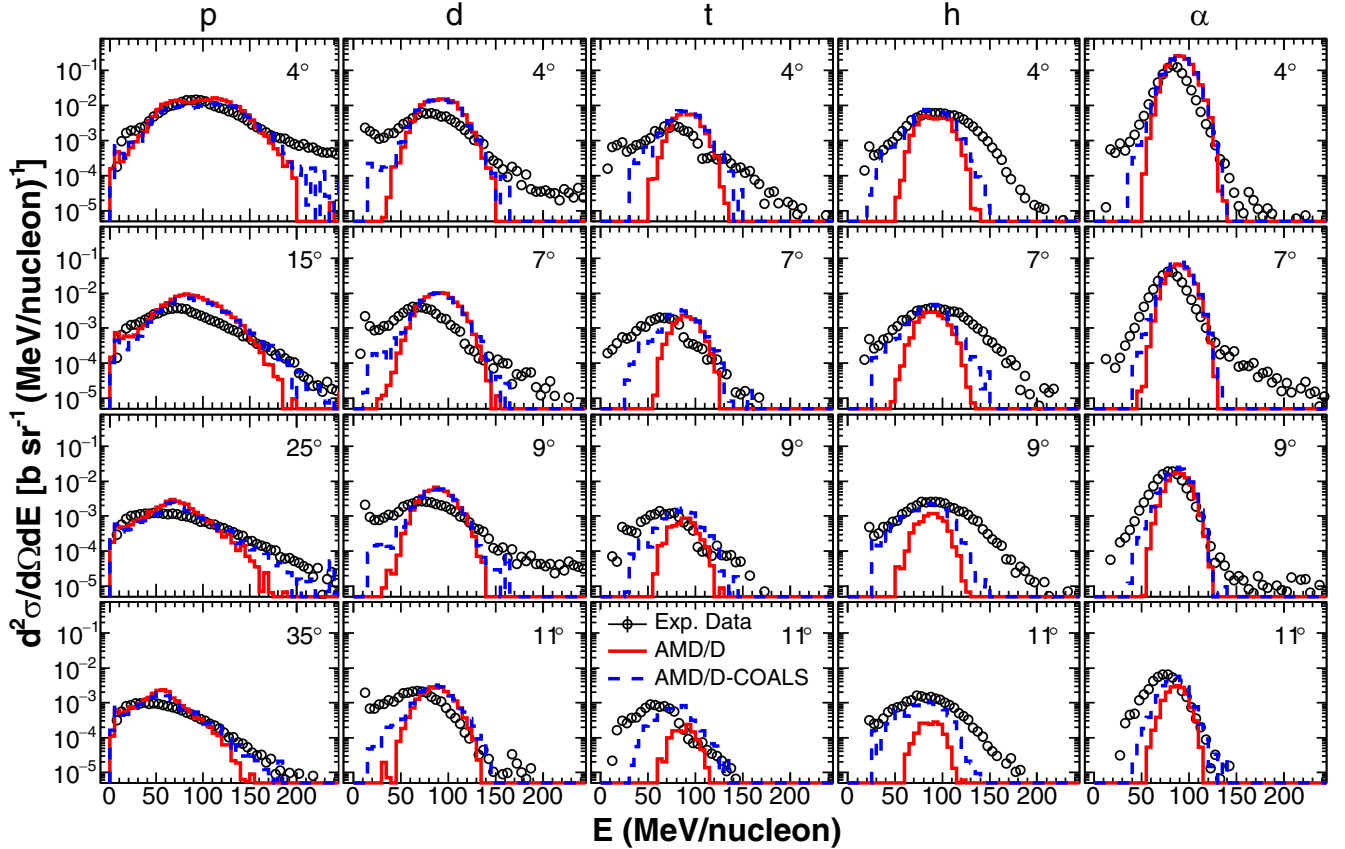


FIG. 4. Comparisons of energy spectra of LCPs between the experimental data and the secondary simulated results with AMD/D and AMD/D-COALS. Four most forward angles are selected for clusters, just because of the poor statistics at larger angles for these LCPs. The experimental data, taken from Ref. [18], are shown by black open circles. Error bars given in the reference are omitted for clarity. The calculated results of AMD/D and AMD/D-COALS are shown by red solid and blue dashed histograms, respectively.

boost (not shown). This is because the Fermi boost is based on the number of collisions, and they become significantly smaller in  $^{12}\text{C} + ^1\text{H}$ . In the coalescence process, when a cluster is formed, the reduced excitation energy is distributed to the surrounding nucleons in the procedure of the total energy restoration. This accelerates protons when the energy is given to the forward emitted protons near the cluster, as shown in the bottom row of Fig. 3. When the free  $NN$  cross sections are used as the input value of the in-medium  $NN$  cross section, the calculated proton energy spectra significantly overpredict on the higher energy side, especially at angles around  $20^\circ$ .

The emission rate of protons also provides information for the effective in-medium  $NN$  cross sections in the binary collision process. The effective in-medium cross sections depend on the input values and Pauli-blocking rate. The latter is determined by the available phase space and depends on how the Pauli principle is treated. In AMD, the Pauli principle is fully respected during the time evolution of the wave packet and collision process, based on the antisymmetrization of the wave packet.

At the top of Fig. 8, the numbers of attempted ( $N_{\text{TRY}}$ ) and Pauli-allowed ( $N_{\text{DID}}$ ) collisions are plotted as a function of the relative nucleon energy for proton-neutron ( $np$ ), and neutron-neutron ( $NN$ ) or proton-proton ( $pp$ ), separately, for the AMD/D-COALS simulations with the default  $NN$  cross

section in Eq. (1). The enhancement around the beam energy is caused by the quasielastic collisions between one of the projectile nucleons and the target proton. Since one of the nucleons is often scattered in free space for the quasielastic collisions, the collisions are more favorably Pauli allowed. The quasielastic contributions are distributed in a broad energy range between  $\approx 95$  and  $\approx 130$  MeV on top of the logarithmically decreasing yields, which is extended above 95 MeV to higher energy under the quasielastic contribution. These higher energy protons correspond to those observed as the high energy component of the energy spectra in Fig. 7. The broad quasielastic peak is caused by the fact that the projectile proton momentum is fluctuated by the quantum diffusion process along the Gaussian distribution and causes the energy spread at this energy range. Therefore the whole of the enhanced yields in this energy range are from the quasielastic scattering. The collisions below  $\approx 95$  MeV and above  $\approx 130$  MeV occur inside the projectile at later stages with a quasiscattered nucleon, and therefore these collisions reflect the effective  $NN$  collision process in the nuclear medium at a given relative kinetic energy.

The effective in-medium  $NN$  cross section can be calculated as

$$\sigma_x^{\text{in-med}}(E) = \sigma_x(\text{LM}; E, \rho) N_{\text{DID}}(x, E) / N_{\text{TRY}}(x, E), \quad (4)$$

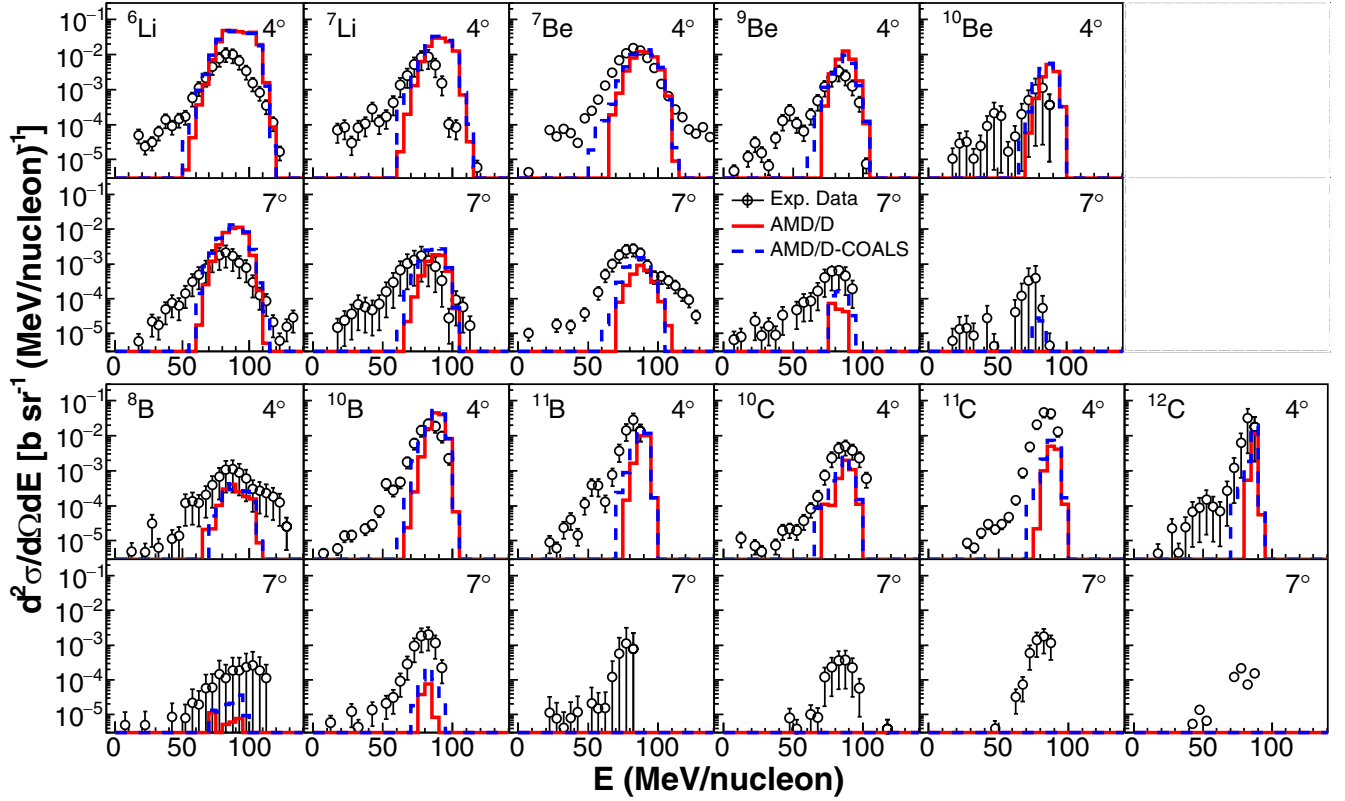


FIG. 5. Similar plots to Fig. 4, but for Li and Be isotopes in the upper two panels, and B and C isotopes for the lower two panels. Symbols and histograms are same as those in Fig. 4.

where the subscript  $x$  indicates either  $np$  or  $nn/pp$ . The LM cross section used in Eq. (1) is energy and density dependent. In the above equation,  $\sigma_x(\text{LM}; E, \rho)$  is the actual cross section calculated when a binary collision occurs with the relative kinetic energy  $E$  and at the density  $\rho$ . The ratio of  $N_{\text{DID}}/N_{\text{TRY}}$  as a function of energy is plotted in Fig. 8(b). About 10–20% of the attempted collisions are Pauli allowed outside the quasielastic region. The calculated effective in-medium cross sections using Eq. (4) are plotted in Fig. 8(c) for  $np$  and  $nn/pp$  collisions separately. The cross sections in the quasielastic region show more or less flat distribution in (b) and (c) as expected. In the energy range  $60 < E < 95$  MeV, the evaluated  $np$  cross sections appear about twice larger than those of  $nn/pp$  and become comparable below 60 MeV.

The evaluated effective in-medium  $NN$  cross sections are compared with the experimental values. At GANIL, a series of the INDRA experiments with symmetric or nearly symmetric reaction systems in the incident energy range of  $20 \leq E \leq 100$  MeV/nucleon have been analyzed [15–17]. The experimental in-medium  $NN$  cross sections are extracted from the measured nuclear stopping values from the high charged multiplicity events. The nuclear stopping is defined as the ratio of the perpendicular and parallel energies in event-by-event basis. Two methods are applied to evaluate the experimental in-medium  $NN$  cross section from the measured proton nuclear stopping values. In the first attempt, the system size independent mean free path is extracted, considering the probable nuclear transparency between the projectile and

target and the Pauli blocking [16]. This system-size independent mean free path is also called the mean free path in nuclear matter, which is directly related to the in-medium  $NN$  cross section. The extracted values are plotted in Fig. 8(c) by the solid symbols. The experimentally extracted values are weight-averaged in-medium cross section between  $np$  and  $nn/pp$  collisions and not directly compared to the values evaluated from the AMD simulations plotted for  $np$  and  $nn/pp$  collisions separately in the figure, but the experimental values are between the values for these collisions, indicating they are very reasonable. The other method is based on the values from the “rows on rows” model of [29] based on the Glauber assumption [30], compared to the measured proton nuclear stopping [17]. In this latter method, the system size dependent in-medium cross sections are evaluated.

To make more direct comparisons between the calculated values and the experimental values, the AMD effective in-medium cross sections are calculated in a similar way as Eq. (4), but using the weight average between  $np$  and  $nn/pp$  collisions as

$$\begin{aligned} \sigma_{\text{AMD}}^{\text{in-med}} = & \sigma_{np}(\text{LM})N_{\text{DID}}(np)/N_{\text{TRY}}^{\text{tot}} \\ & + \sigma_{nn/pp}(\text{LM})N_{\text{DID}}(nn/pp)/N_{\text{TRY}}^{\text{tot}}, \end{aligned} \quad (5)$$

where  $N_{\text{TRY}}^{\text{tot}} = N_{\text{TRY}}(np) + N_{\text{TRY}}(nn/pp)$ .

The effective AMD in-medium  $NN$  cross sections are evaluated using Eq. (5). In Fig. 9(a), the values from Eq. (1) are plotted for the density indicated, together with the

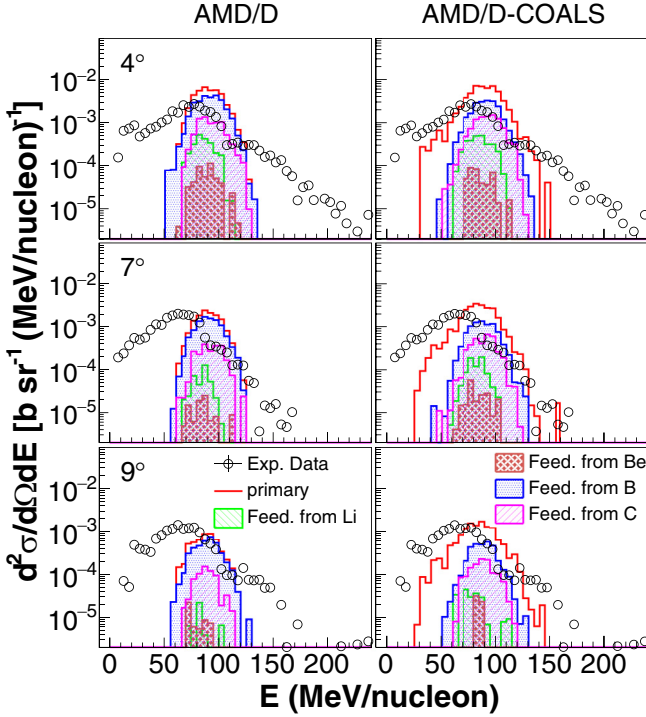


FIG. 6. Energy spectra of tritons at three selected angles,  $4^\circ$ ,  $7^\circ$ ,  $9^\circ$ , are compared with the simulations from AMD/D on the left and AMD/D-COALS on the right. The experimental data are same on both sides and shown by black open circles. The results obtained from the simulations are shown by the red solid histograms. The feeding contributions from Li, Be, B, and C parent isotopes are also shown by colored shaded spectra. No error bars are shown for the experimental data.

parametrized experimental free  $NN$  cross sections. The cross sections in Eq. (1) are determined by the empirical values below 90 MeV for  $np$  collisions.  $nn/pp$  collisions are determined by the LM formulation above 20–30 MeV, but are a factor of more than 2 smaller than those of the  $np$  cross sections. In Fig. 9(b) the calculated AMD effective in-medium cross sections are compared to the experimental values from Ref. [16], which are independent of the system size. The AMD values agree surprisingly well with the experimental values in the whole energy range except at the beam energy, especially the minimum observed around 40 MeV, and the rise at lower energy is also well reproduced. To show the effective in-medium values for the AMD simulation around the beam energy, the incident energy is artificially increased to 130 MeV/nucleon for the same reaction and is shown in Fig. 9(c). Now one can see that the AMD effective in-medium  $NN$  cross section is extended up to 120 MeV with almost constant values above 90 MeV, and the experimental value at 100 MeV is only slightly underpredicted. The target size dependent cross sections from Ref. [17] are also shown by colored symbols above 40 MeV/nucleon, but they are slightly larger than the AMD values. To see the dependence of the resultant AMD in-medium  $NN$  cross section on the input in-medium cross section, the free  $NN$  cross sections are used at 95 MeV/nucleon.

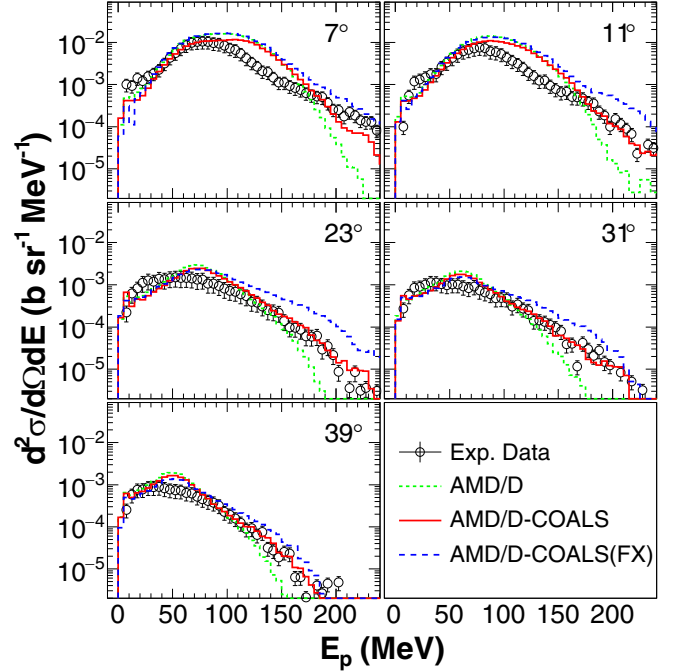


FIG. 7. Typical proton energy spectra at selected angles with AMD/D and AMD/D-COALS. In AMD/D-COALS(FX), the free  $NN$  cross sections are used.

The results are shown in Fig. 9(d). The calculated AMD in-medium cross section is overpredicted below 50 MeV by a factor of more than 2–3. In the energy range of  $70 \leq E \leq 90$  MeV, on the other hand, the input cross sections are larger by about a factor of 2, compared to the values of Eq. (1), but the resultant AMD cross sections are comparable to those in (b) at this energy range. This indicates that the increase of the input cross section by up to a factor of 2 can be adjusted by the increase of the Pauli blocking, but it breaks down when the increase becomes more than by a factor of 2–3.

## V. SUMMARY

Three AMD models, AMD/noD, AMD/D and AMD/D-COALS are compared in detail with the experimental data of  $^{12}\text{C} + ^1\text{H}$  at 95 MeV/nucleon, focusing on the stochastic processes of the diffusion and coalescence processes and binary collisions with different in-medium cross sections. The simulated 2D velocity plots reveal well the role of each incorporated process. The experimental energy spectra of LCPs and IMFs are compared with those of the AMD simulations. The role of the coalescence model is clarified. These additional processes improve the reproduction of these spectra, but still some discrepancies remain between the calculations and experimental data. The following observations are obtained in these comparisons.

- (i) For protons overall shapes of the energy spectra are well reproduced. At angles larger than  $15^\circ$  with AMD/D-COALS, noticeable underpredictions are observed for these high energy components without the coalescence process.

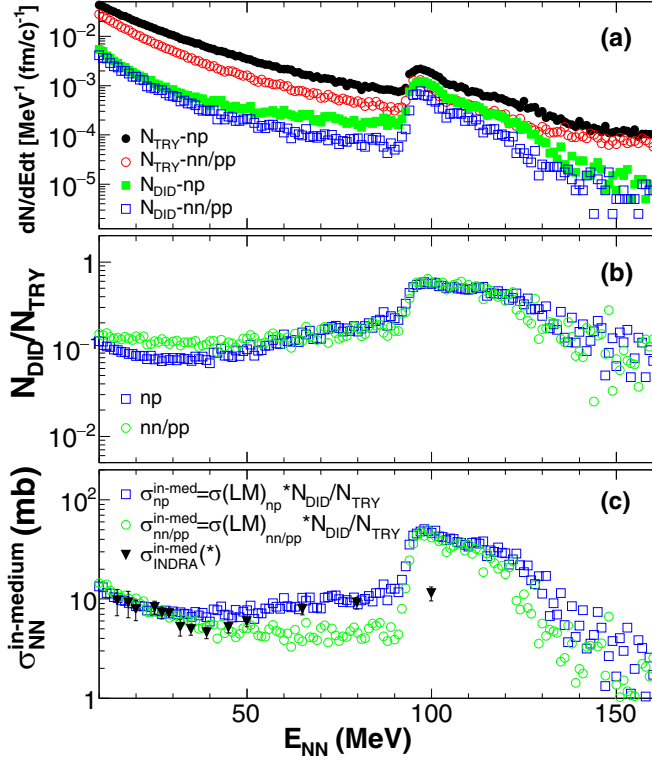


FIG. 8. (a) Number of attempted ( $N_{\text{TRY}}$ ) and Pauli-allowed ( $N_{\text{DID}}$ ) collisions for the binary collisions of proton-neutron ( $np$ ) and neutron-neutron ( $nn$ ) pairs as a function of the relative nucleon energy.  $pp$  collisions are same as  $nm$  ones. Black and green symbols are  $N_{\text{TRY}}$  and  $N_{\text{DID}}$  for  $np$  collisions, respectively. Red and blue are those for  $nn$  or  $pp$  collisions. (b) Ratio of  $N_{\text{DID}}$  and  $N_{\text{TRY}}$  from (a). (c) Calculated in-medium cross sections for  $np$  and  $nn/pp$ , using the formula indicated in the figure. See details in the text. The triangle symbols are the results from Ref. [16].

- (ii) The high energy tails above 200 MeV observed in the proton spectra at angles below  $13^\circ$  are attributed to problems in the experimental analysis procedure, such as poor energy calibration.
- (iii) For light clusters, the low energy yields are significantly improved with the coalescence process, but high energy yields above 150 MeV/nucleon remain unexplained by both AMD/D and AMD/D-COALS. These could be caused by the same problem as that of protons, but need to be verified with further experiments.
- (iv) The energy spectra of deuterons and tritons show significant overprediction for the PLF component with both AMDs, which is caused by the sequential decay of excited IMFs. The extension of the coalescence process for  $4 < A < 8$ , however, does not improve significantly these yields, compared to the previous study in Refs. [11–13].
- (v) The PLF component of IMF yields are well reproduced with both AMDs.
- (vi) The low energy yields observed below 50 MeV/nucleon are not explained with both AMDs.

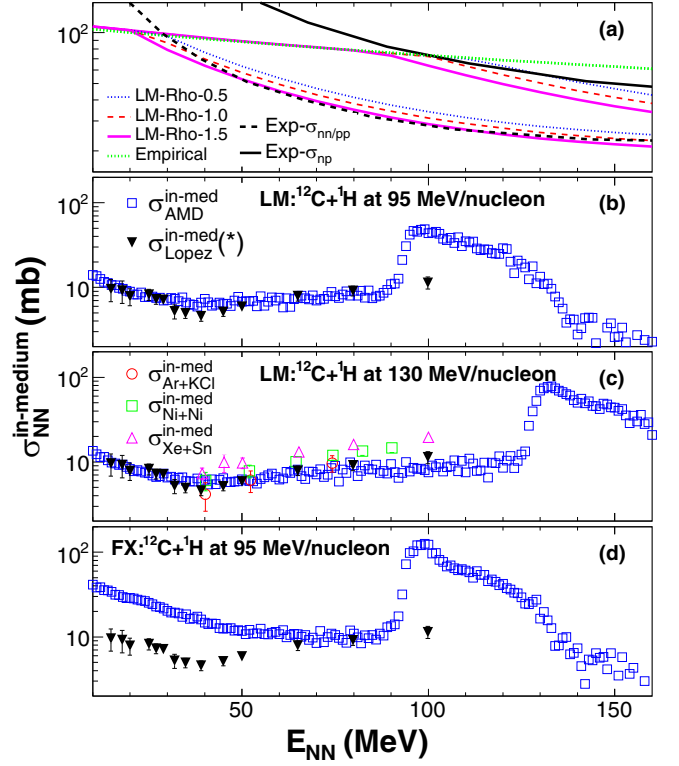


FIG. 9. (a) In-medium  $NN$  cross sections used as the input values in the AMD simulations as a function of the relative nucleon energy. Colored curves correspond to those from Eq. (1) at a given density  $\rho$  indicated in the figure. Black solid and dashed curves are the fitted experimental free  $np$  and  $nn/pp$  cross sections. The green dotted line indicates the empirical in-medium cross sections. (b) Calculated AMD in-medium cross section from Eq. (5) for  $^{12}\text{C}+^1\text{H}$  at 95 MeV/nucleon. The solid triangle symbols are the experimental values from Ref. [16]. (c) Similar plot to (b), but for  $^{12}\text{C}+^1\text{H}$  at 130 MeV/nucleon. Colored symbols are the experimentally extracted values from Ref. [17]. They are system-size dependent as indicated by the reaction system. (d) Similar plot to (c), but using the free  $NN$  cross sections for the collision process, shown by black curves in (a). The solid symbols are the same as those in (b).

These could be caused by the subtraction procedure between  $^{12}\text{C} + \text{C}$  and  $^{12}\text{C} + \text{CH}_2$  reactions.

- (vii) The effective in-medium  $NN$  cross sections are evaluated from the AMD simulations and they agree well with the experimentally extracted values in the available energy range.

## ACKNOWLEDGMENTS

The authors thank Dr. A. Ono for providing us his AMD codes (AMD/noD, AMD/D, and AMD/D-COALS) and for stimulating discussions and comments. This work is supported by the National Natural Science Foundation of China (Grants No. U1832205, No. 11875298, No. 12005265) and the CAS “Light of West China” Program (Grant No. 29Y725030). This work is also supported by the U.S. Department of Energy under Grant No. DE-FG02-93ER40773.

- [1] H. Wolter *et al.*, *Prog. Part. Nucl. Phys.* **125**, 103962 (2022), and references therein.
- [2] J. Xu, L.-W. Chen, M. B. Tsang, H. Wolter, Y.-X. Zhang, J. Aichelin, M. Colonna, D. Cozma, P. Danielewicz, Z.-Q. Feng, A. L. Fèvre, T. Gaitanos, C. Hartnack, K. Kim, Y. Kim, C.-M. Ko, B.-A. Li, Q.-F. Li, Z.-X. Li, P. Napolitani, A. Ono *et al.*, *Phys. Rev. C* **93**, 044609 (2016).
- [3] M. Colonna, Y.-X. Zhang, Y.-J. Wang, D. Cozma, P. Danielewicz, C. M. Ko, A. Ono, M. B. Tsang, R. Wang, H. Wolter, J. Xu, Z. Zhang, L.-W. Chen, H.-G. Cheng, H. Elfner, Z.-Q. Feng, M. Kim, Y. Kim, S. Jeon, C.-H. Lee *et al.*, *Phys. Rev. C* **104**, 024603 (2021).
- [4] Y.-X. Zhang, Y.-J. Wang, M. Colonna, P. Danielewicz, A. Ono, M. B. Tsang, H. Wolter, J. Xu, L.-W. Chen, D. Cozma, Z.-Q. Feng, S. D. Gupta, N. Ikeno, C.-M. Ko, B.-A. Li, Q.-F. Li, Z.-X. Li, S. Mallik, Y. Nara, T. Ogawa, A. Ohnishi *et al.*, *Phys. Rev. C* **97**, 034625 (2018).
- [5] A. Ono, J. Xu, M. Colonna, P. Danielewicz, C. M. Ko, M. B. Tsang, Y.-J. Wang, H. Wolter, Y.-X. Zhang, L.-W. Chen, D. Cozma, H. Elfner, Z.-Q. Feng, N. Ikeno, B.-A. Li, S. Mallik, Y. Nara, T. Ogawa, A. Ohnishi, D. Oliinychenko *et al.*, *Phys. Rev. C* **100**, 044617 (2019).
- [6] A. Ono, H. Horiuchi, T. Maruyama, and A. Ohnishi, *Prog. Theor. Phys.* **87**, 1185 (1992).
- [7] A. Ono and H. Horiuchi, *Phys. Rev. C* **53**, 2958 (1996).
- [8] R. Wada, K. Hagel, J. Cibor *et al.* (The GANIL E-160 Collaboration), *Phys. Rev. C* **62**, 034601 (2000).
- [9] R. Wada, T. Keutgen, K. Hagel *et al.*, *Phys. Rev. C* **69**, 044610 (2004).
- [10] A. Ono, *Prog. Theor. Phys. Suppl.* **140**, 134 (2000).
- [11] G. Tian, R. Wada, Z. Chen, R. Han, W. Lin, X. Liu, P. Ren, F. Shi, F. Luo, Q. Sun, L. Song, and G. Q. Xiao, *Phys. Rev. C* **95**, 044613 (2017).
- [12] G. Tian, Z. Chen, R. Han, F. Shi, F. Luo, Q. Sun, L. Song, X. Zhang, G. Q. Xiao, R. Wada, and A. Ono, *Phys. Rev. C* **97**, 034610 (2018).
- [13] R. Han, Z. Chen, R. Wada, A. Ono, G. Tian, F. Shi, X. Zhang, B. Liu, and H. Sun, *Phys. Rev. C* **102**, 064617 (2020).
- [14] A. Ono, H. Horiuchi, and T. Maruyama, *Phys. Rev. C* **48**, 2946 (1993).
- [15] G. Lehaut, D. Durand, O. Lopez, E. Vient, A. Chbihi, J. D. Frankland, E. Bonnet, B. Borderie, R. Bougault, E. Galichet, D. Guinet, Ph. Latusse, N. Le Neindre, P. Napolitani, M. Parlog, M. F. Rivet, and E. Rosato (INDRA and ALADIN Collaborations), *Phys. Rev. Lett.* **104**, 232701 (2010).
- [16] O. Lopez, D. Durand, G. Lehaut, B. Borderie, J. D. Frankland, M. F. Rivet, R. Bougault, A. Chbihi, E. Galichet, D. Guinet, M. La Commara, N. Le Neindre, I. Lombardo, L. Manduci, P. Marini, P. Napolitani, M. Pârlog, E. Rosato, G. Spadaccini, E. Vient, and M. Vigilante (INDRA Collaboration), *Phys. Rev. C* **90**, 064602 (2014).
- [17] M. Henri, O. Lopez, D. Durand, B. Borderie, R. Bougault, A. Chbihi, Q. Fable, J. D. Frankland, E. Galichet, D. Gruyer, J. Lemarié, N. Le Neindre, I. Lombardo, M. Pârlog, J. Quicray, G. Verde, E. Vient, and M. Vigilante (INDRA Collaboration), *Phys. Rev. C* **101**, 064622 (2020).
- [18] J. Dudouet, D. Juliani, M. Labalme, D. Cussol, J. C. Angélique, B. Braunn, J. Colin, Ch. Finck, J. M. Fontbonne, H. Guérin, P. Henriquet, J. Krimmer, M. Rousseau, M. G. Saint-Laurent, and S. Salvador, *Phys. Rev. C* **88**, 024606 (2013).
- [19] A. Ono and H. Horiuchi, *Phys. Rev. C* **53**, 845 (1996).
- [20] A. Ono and H. Horiuchi, *Phys. Rev. C* **53**, 2341 (1996).
- [21] A. Ono, S. Hudan, A. Chbihi, and J. D. Frankland, *Phys. Rev. C* **66**, 014603 (2002).
- [22] G. Q. Li and R. Machleidt, *Phys. Rev. C* **48**, 1702 (1993).
- [23] G. Q. Li and R. Machleidt, *Phys. Rev. C* **49**, 566 (1994).
- [24] J. Dechargé and D. Gogny, *Phys. Rev. C* **21**, 1568 (1980).
- [25] R. J. Charity, M. A. McMahan, G. J. Wozniak, R. J. McDonald, L. G. Moretto, D. G. Sarantites, L. G. Sobotka, G. Guarino, A. Pantaleo, L. Fiore, A. Gobbi, and K. D. Hildenbrand, *Nucl. Phys. A* **483**, 371 (1988).
- [26] B. J. Fineman, K.-T. Brinkmann, A. L. Caraley, N. Gan, R. L. McGrath, and J. Velkovska, *Phys. Rev. C* **50**, 1991 (1994).
- [27] C. Divay, J. Colin, D. Cussol, Ch. Finck, Y. Karakaya, M. Labalme, M. Rousseau, S. Salvador, and M. Vanstalle, *Phys. Rev. C* **95**, 044602 (2017).
- [28] W. Lin, X. Liu, R. Wada, M. Huang, P. Ren, G. Tian, F. Luo, Q. Sun, Z. Chen, G. Q. Xiao, R. Han, F. Shi, J. Liu, and B. Gou, *Phys. Rev. C* **94**, 064609 (2016).
- [29] J. Hüfner and J. Knoll, *Nucl. Phys. A* **290**, 460 (1977).
- [30] R. J. Glauber and G. Matthiae, *Nucl. Phys. B* **21**, 135 (1970).